

Bearing capacity of micropiled-raft system

Tae-Hyun Hwang^a, Kang-Hyun Kim^b and Jong-Ho Shin*

Department of Civil Engineering, Konkuk University, 120 Neungdong-ro, Gwangjin-gu, Seoul 05029, Republic of Korea

(Received September 26, 2016, Revised May 30, 2017, Accepted May 31, 2017)

Abstract. The micropile has been mainly used under the concept of supplementing structural support or reinforcing soft ground. For the micropiled-raft system which uses a micropile and a raft in combination in particular, it is generally considered as ground reinforcement rather than foundation components considering the bearing capacity of the micropile in many cases. In this study, the bearing capacity mechanism of the micropiled-raft system is investigated through a physical model test and numerical method. The numerical results have shown that not only the slender-pile-effect of the micropile, but also the ground reinforcement effect, increase the bearing capacity considerably. The bearing capacity formula of the micropiled-raft system is derived based on the failure mechanism obtained through model tests. The formula is verified and proposed as a design chart.

Keywords: bearing capacity; micropile; micropiled-raft; numerical analysis; model test; failure mechanism

1. Introduction

The diameter of a micropile is noticeably smaller than that of a general pile, thus its mechanical effect as a structural member has often been ignored. However, according to the experiences of field works, a micropiled-raft system is known to contribute considerably to the bearing capacity of the raft.

A micropile is a grouted column of a steel bar or pipe with a diameter of 300 mm or smaller, and is installed in about 10 to 30 m depth in accordance with the soil condition. Micropiles have been usefully applied to foundation reinforcement for old buildings or to places having constraints in securing the area for foundation (FHWA 2005, Holman 2009, Pinyol *et al.* 2012, Sun *et al.* 2013, Sailsbury and Davidow 2014, Kyung and Lee 2017). As a micropile is slender and has high flexibility, it has been mainly handled under the concept of reinforcing the soil rather than of load bearing. Thus micropiled-raft systems are generally designed under the concept where the contribution of the micropile to bearing capacity is ignored.

As the behavior of a piled raft system is determined by an interaction between the pile and the raft, the behavior of a micropile may not be greatly different from the 'slender pile' of the existing pile design. Accordingly, as to the contribution of a micropile to bearing capacity, the short or slender pile condition of the existing large diameter pile design standard (Poulos and Davis 1980) can be referred to. The contribution of a slender pile to bearing capacity is affected by the rigidity of the soil on which the pile is installed rather than by the length of the pile (Hoalley *et*

al. 1969, Randolph 1994, Meyerhof 1995, Chen *et al.* 2013). As the individual rigidity of a micropile is much smaller than that of a large diameter pile, the ratio of the bearing capacity contributed by the raft may be relatively high in comparison with that of the existing slender pile. However, micropiles are generally installed in groups. Thus the total contribution from the micropile would not be as small.

The structural behavior of a micropile is affected by diverse parameters such as the soil condition, installation interval, length, installation angle, grouting method, pressure level, relative rigidity between the pile and the soil, etc. Meyerhof and Yalcin (1993) reported that the installation length of a slender pile has almost no effect on bearing capacity and has absolutely no effect on bearing capacity if the relative rigidities of the soil and the pile are below a certain value. Thus, for the micropile, the relative rigidity of the soil and the pile and the installation angle are the dominant factors of combined behavior. According to You *et al.* (2003), Tsukada *et al.* (2006), Shu and Muhunthan (2010), Colmenares *et al.* (2014), displacement develops to the ground surface around the foundation during a failure of a micropiled-raft system. Hwang *et al.* (2017) reported that the failure mechanism of micropiled-raft was enlarged as the pile installation angle decreased. In this case, the pile installation angle has an important factor on the bearing capacity.

In this study, the supporting behavior of a micropiled-raft system which is not appropriately considered at the present design practice of the micropile was investigated through a numerical method and physical model test.

2. Load carrying mechanism of micropiled-raft system

2.1 Bearing capacity of a single micropile

Micropiled-raft is a foundation system whose bearing

*Corresponding author, Professor

E-mail: jhshin@konkuk.ac.kr

^aAdjunct Professor

^bPh.D Candidate

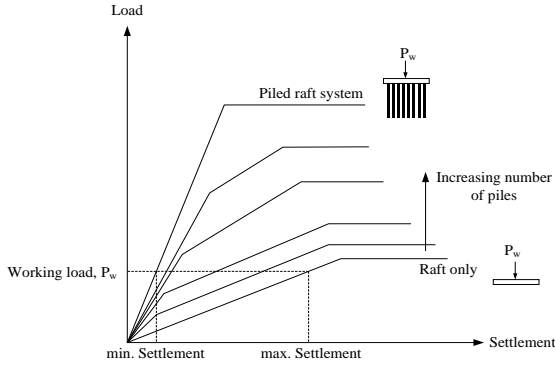


Fig. 1 Concept of piled-raft system (Poulos and Davis 1980)

capacity is obtained from both micropile and raft. The bearing capacity of a single micropile in ductile condition can be obtained by using the bearing capacity equations proposed by Francis (1964).

$$Q_{u(m)} = \frac{\pi^2 \cdot E_p \cdot I_p}{4(S_R + J_R)^2 \cdot R^2} \cdot \cos(\pi/2 - i) \quad (1)$$

Where, $S_R = L_S/R$, $J_R = L_u/R$, $R = \{(E_p \cdot I_p)/(k_h \cdot D)\}^{1/4}$, $L_u = B \cdot \exp\{(\pi/2 - i) \cdot \tan\phi\} \cdot \tan(\pi/4 + \phi/2)$.

$L_s = (\pi/2) \cdot R$ represents the equivalent free length of the embedded depth of the pile, L_u represents the unsupported pile length, and k_h represents the modulus of subgrade reaction. B is the width of the raft, D is the diameter of the micropile, and i is the installation angle.

Meyerhof and Yalcin (1993) defined the relative stiffness of the pile between the soil and pile as $K_r = (E_p \cdot I_p)/(E_s \cdot L^4)$, where the E_p and E_s represent the elastic modulus of the pile and soil respectively, and I_p and L represent the sectional moment of inertia and length of the micropile respectively. In general, if K_r is less than 0.01, the pile shows a ductile behavior and, as the relative rigidity (K_r) of the micropile used in the field is between 0.0018 and 0.0065, it falls under ductile condition.

The bearing capacity $Q_{u(m)}$ of the micropile is related with the installation length, and is a function of the pile cross section, relative rigidity between the soil and the pile, and installation angle.

2.2 Bearing capacity of micropiled-raft

The bearing capacity of a piled-raft system is proposed by Poulos and Davis (1980), Reul and Randolph (2003), Sanctis and Mandolini (2006), Aluaim *et al.* (2015), Saha *et al.* (2015) as shown in Fig. 1. The concept can be presented as the following equation

$$Q_{u(mr)} = Q_{u(r)} + N \cdot Q_{u(m)} \quad (2)$$

N represents the number of micropiles, $Q_{u(mr)}$ represents the bearing capacity of the piled-raft system, and $Q_{u(r)}$, $Q_{u(m)}$ represent the bearing capacities of a raft and vertical piles respectively. In Eq. (2), $Q_{u(m)}$ can be evaluated using the existing theory of the slender pile.

Eq. (2) is basically driven for the vertical and large diameter of pile of which bearing capacity is significantly

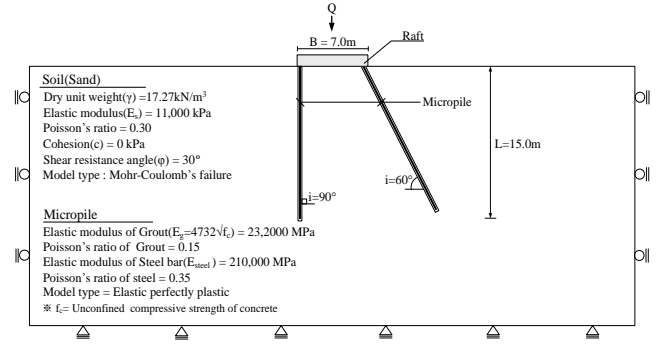


Fig. 2 Analysis model and material parameters

larger than that of the raft. Meanwhile the micropile is considerably flexible and generally installed with some slope. Bearing capacity of individual micropile, $Q_{u(m)}$ can be evaluated using Eq. (1) considering installation angle of i . However, the bearing capacity from the raft, $Q_{u(r)}$, cannot be simply evaluated because the micropile modifies the failure mechanism significantly.

2.3 Numerical investigation of the behavior of the micropiled-raft

In order to investigate the load carrying mechanism of the micropiled-raft system, a two-dimensional plane strain model based on plane strain condition was considered. The finite element program to use for analysis is MIDAS GTS (2010). Fig. 2 shows the numerical model of a micropiled-raft system where two rows of micropiles are installed beneath a raft on sand. Micropiles of 150 mm diameter and 15 m length are vertically installed beneath a spread footing of 7 m width, with the installation interval at 0.6 m. Two cases of installation angle are considered: 90°, and 60°. The soil was modeled using the elastoplastic material of Mohr-Coulomb model, and micropile was modeled using an elastic bar element. To consider the interface behavior between micropile and soil, interface elements were adopted.

There may be several ways to determine the ultimate bearing capacity from the numerical results. According to Lamb and Whitman (1979), Das (2011), in the medium dense sand the load-displacement does not appear peak stress due to its ductile behavior. In this case, the ultimate load bearing capacity is obtained generally for too large settlement exceeding allowable settlement. To avoid the problem, displacement based bearing capacity in which local shear failure occurs was proposed by Das (2011). He suggested the 10% strain as the corresponding strain for the bearing resistance. The load-displacement behavior was investigated in three conditions, 'micropile only', 'raft only' and 'micropiled-raft'. The analyses were carried out until the vertical strain exceeded 10% of the foundation width by increasing the vertical displacement of the raft by 10 mm at each analysis increment. The results of analyses presented in terms of a load-settlement curve are shown in Fig. 3(a). It is shown that the load carried by the micropiled-raft system continuously increased even after the micropile reached the yield point.

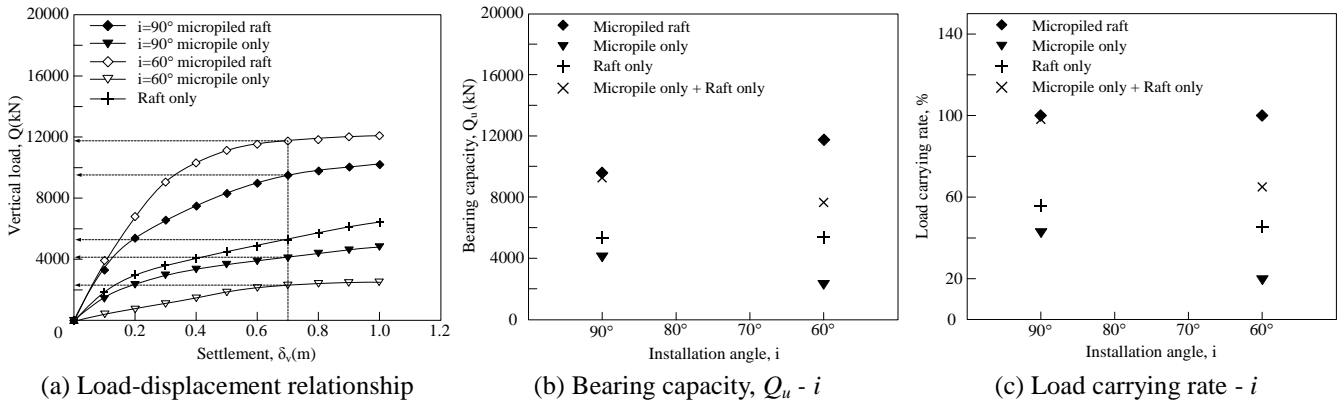


Fig. 3 Numerical simulation of bearing resistance of micropiled-raft

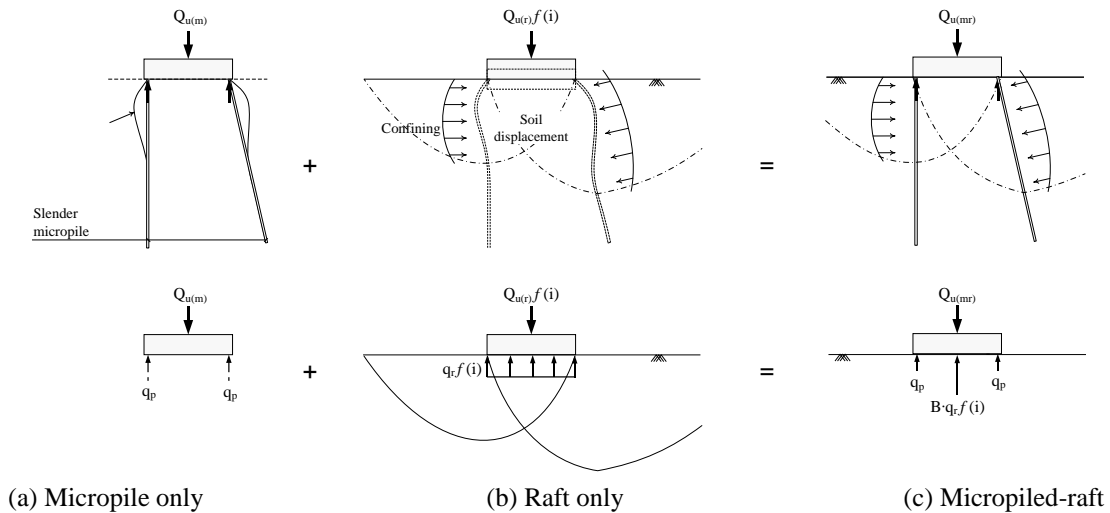


Fig. 4 Mechanism of bearing resistance of micropiled-raft system

The bearing capacities of the raft, the micropile and the micropiled-raft were shown to be 5350 kN, 4130 kN, and 9610 kN respectively at the installation of 90°. And those for installation of 60° were 5350 kN, 2310 kN and 11760 kN respectively. It is interesting to note that the bearing capacity of the micropiled-raft system is similar to the simple sum of the individual bearing capacities of the micropiles and raft at the installation of 90° as shown in Fig. 3(b). However, in case of $i=60^\circ$, although the bearing capacity of micropiles has decreased the bearing capacity of micropiled-raft is much higher than the simple sum of individual micropiles and raft by about 34.9%. This is because micropiles contributed to increase in the bearing capacity of the raft by reinforcing ground. And this means that the bearing capacity of micropiled-raft is dependent on the installation angle.

When a load is applied to a micropiled-raft system, as the rigidity of the pile is higher than that of the soil, the micropile comes to bear the load first. Accordingly, the micropile reaches the yield state before the soil beneath the raft does. After yielding, the micropile contributes to increase in the load carrying capacity of the raft by confining the soil beneath the foundation. Such a failure mechanism of a micropiled-raft system indicates that the load carrying capacity of a micropiled-raft system can be

appropriately considered by superposition of the slender pile effect of the micropile and the reinforcement effect of the foundation soil.

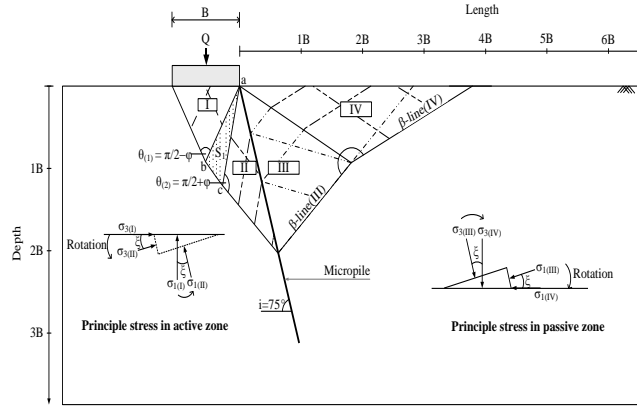
The modified failure mechanism indicates that the Eq. (2) proposed for the large and stiff piled-raft is not valid to the micropiled-raft. The reinforcement effect of ground can be considered by evaluating $Q_{u(r)}$, for the modified mechanism due to micropiles and the bearing capacity equation of the micropiled-raft system can be inferred as shown in Fig. 4.

The $Q_{u(r)}$ depends on the installation angle which is the crucial factor modifying the failure mode: $Q_{u(r)}:f(i)$. The bearing capacity of a micropiled-raft system is now can be written as the sum of its bearing capacity as a slender pile and the raft bearing capacity of the soil reinforced by the micropile.

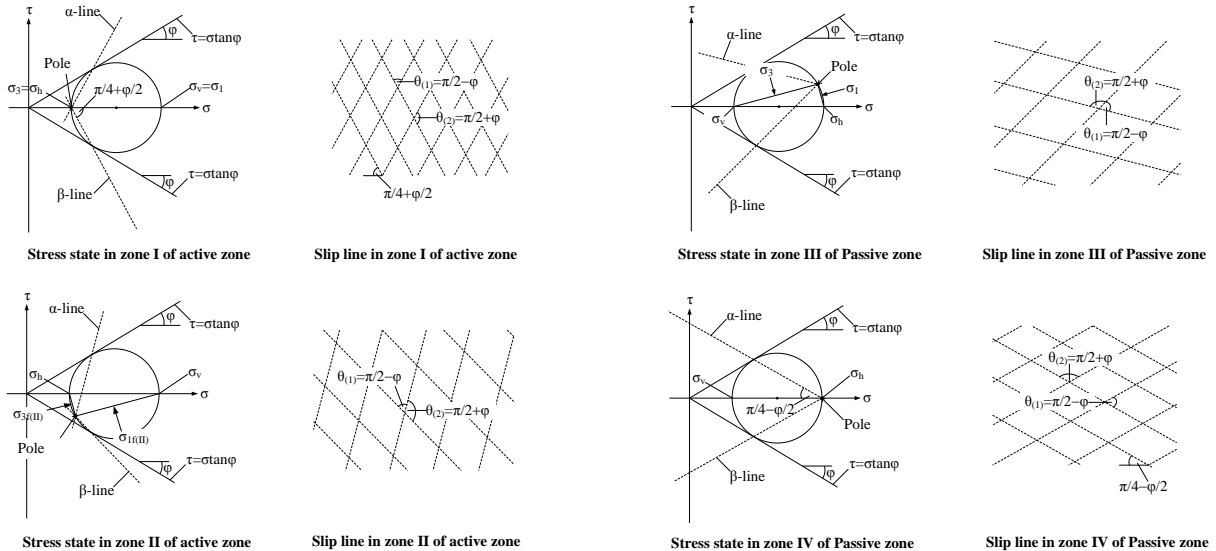
This indicates that the reinforcing effect of micropile can be taken into account by considering failure mechanism of the reinforced ground.

3. Model test and failure mode of micropiled-raft

To obtain bearing capacity equation, the upper bound analysis of limit theorem is adopted in this study. The basic



(a) Potential failure surface ($i=75^\circ$)



(b) Stress state and slip lines

Fig. 5 Comparison with the failure surface

assumption of this theory are that the whole soil mass is in the rigid perfectly plastic condition, only the starting

$$Q_{u(mr)} = Q_{u(r)} \cdot f(i) + N \cdot Q_{u(m)} \quad (3)$$

moment of failure is considered. It assumes that there exists a dynamically admissible strain field in which external works are equivalent to internal strain energy. The theoretical bearing capacity can be obtained when the lower bound solution becomes equal to the upper bound solution in the limit theorem.

However, as the boundary condition of the micropiled-raft system is very complicated, it is not easy to carry out zoning to obtain the lower bound solution. In addition, there is no sufficient known information about the failure mode for the upper bound solution. In this study, model tests for the micropiled-raft system were performed and the bearing capacity was calculated using the upper bound solution for the failure mode obtained from the model test. In order to estimate the approximate failure zone before carrying out the model test, the theoretical failure mode was evaluated using the origin of plane of the Mohr circles (Harr 1966, Tschebotarioff 1973, Chen 1975, Das 2011) as shown in Fig. 5(a).

Failure surface can be determined using poles of Mohr circle. It can be simply recognized that the micropile introduces the boundary between active and passive zones exist. Battered installation of micropile changes the failure surface, which in turn rotates principle stress and causes β -line failure surface. Slip lines appear in 4 zones are illustrated in Fig. 5(b).

In Fig. 5(a), zone I can be assumed to be a rigid wedge, zone II a shear fan (zone I and zone II in combination are also called the active zone of Rankine), and zones III and IV can be assumed to be the passive zones of Rankine. The failure zone varies depending on the installation angle of the micropile. An actual failure mode to apply for the upper bound solution can be derived by comparatively analyzing this theoretical failure mode with the failure modes obtained from model tests. The size of the soil box and the soil layer for model tests were established based on the theoretical failure model shown in Fig. 5(a).

3.1 Model tests on micropiled-raft system

In order to determine the failure mechanism of a micropiled-raft system in the soil, a model tester was

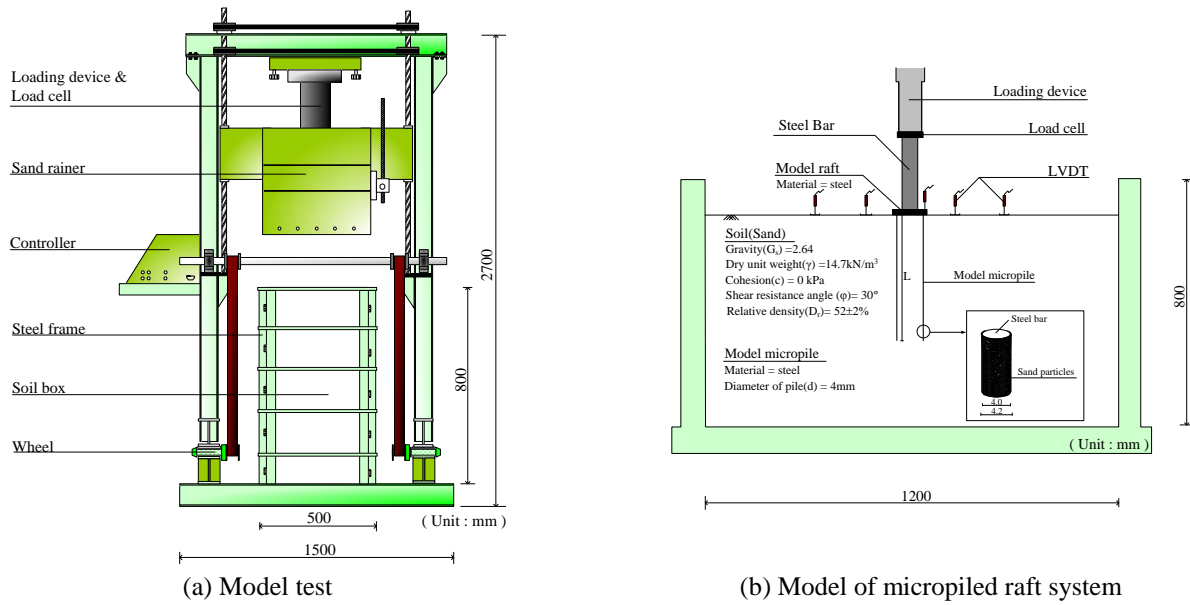


Fig. 6 Model test device

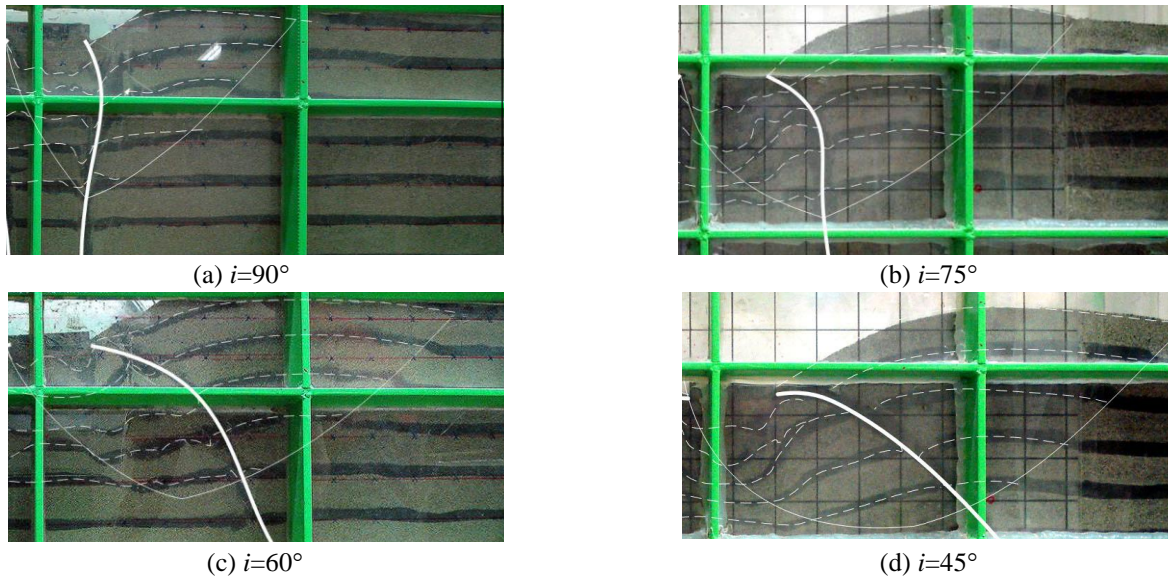


Fig. 7 Observed failure modes

devised as shown in Fig. 6. The size of the soil box installed in this tester was 1200×500×800 (length×width×height, mm). The soil was dried sand with a uniformity coefficient, C_u of 1.62 and coefficient of curvature, C_g of 0.87, and the soil in the model container was homogeneously built to have about 50% relative density using a ‘soil rainer’. Also, to enable the failure mode of the soil beneath the foundation system to be observed visually, a thin black sand layer was laid at a regular interval of 10 mm.

As the supporting characteristics of the pile is mainly dependent on the flexural rigidity of the pile, the diameter of the model pile was determined by considering the following relative rigidity to secure the similarity between the model and prototype.

$$\lambda_{EI} = \frac{E_p I_p}{E_m I_m} = \lambda_L^5 \quad (4)$$

Where the subscripts p and m represent the prototype and model respectively. According to Iai (1989), Iai *et al.* (2005), the λ_L (length scale) for the micropile is about 1/20. The prototype micropile is a grouted steel bar (or pipe) 200 mm in diameter widely used in the field, and the model pile was set to be a 4 mm diameter wire made of steel. Soil particles are attached to the surface of the model micropile as shown in Fig. 6(b) in order to introduce the frictional interface on the boundary surface between the soil and the micropile (Tsukada *et al.* 2006). Model tests were conducted for the installation angle of 45°, 60°, 75° and 90°. In each test, a load was applied until the ratio of vertical displacement to the width of the foundation, that is to say, the vertical strain, exceeded 10% which is considered as a state of failure (Han and Ye 2006).

3.2 Failure mechanism of micropiled-raft

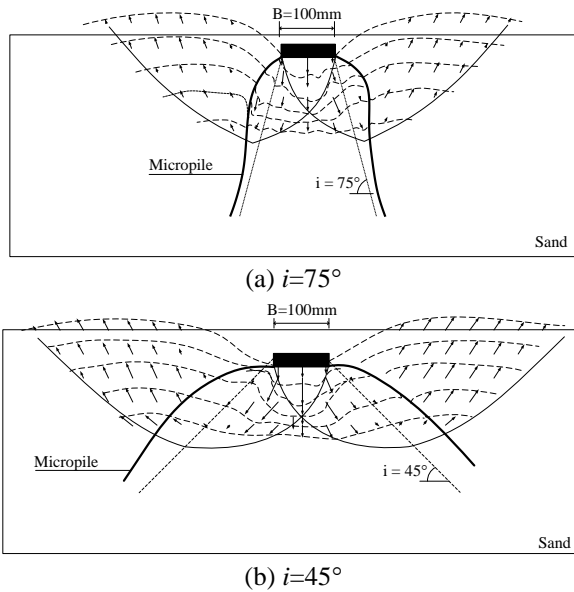


Fig. 8 Failure mechanisms for varying installation angle

The 10% axial strain was set as the reference of failure, and the failure mode was investigated at this strain. Fig. 7 shows the micropiled-raft system at failure. Fig. 7 shows that the micropile has deflected considerably after the test and failure of the foundation soil was clearly identified. Significant slips in dark sand layers indicate a failure surface. Fig. 8 illustrates the failure shape and the displacement vectors for different installation angles. The rigid wedge and the passive zone are shown to be clearly divided by the micropile. The size of the soil failure area varies in accordance with the installation angle, and it has been shown that, the bigger the installation angle is, the more the soil failure area expands.

When the observed failure mode shown in Fig. 8 is compared with the theoretical failure mode in Fig. 5 as shown in Fig. 9, the failure zones between the foundation and the micropile (soils in zones I and II and shear fan zone) in the theoretical failure mode and the measured failure mode have generally shown to be similar in size and shape. However, the test result in the passive zone (soil in

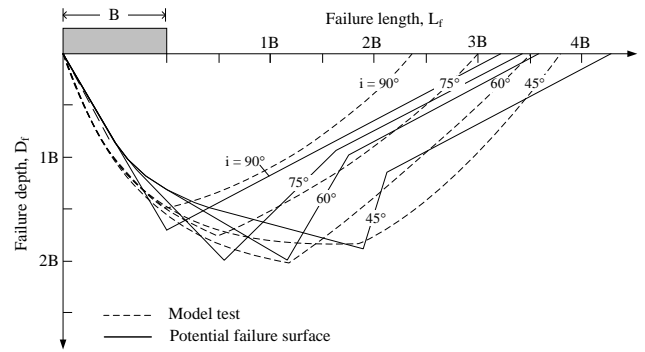


Fig. 9 Comparison of failure mechanisms

zone III and IV) has shown a difference from that of the theoretical failure mode. This is because the theoretical approach has not appropriately considered the effect of rotation on the principal stress, which caused by the ground reinforcement.

The relation between the contained angles $\theta_{(1)}$ and $\theta_{(2)}$ of the passive zones III and IV in Fig. 5 does not satisfy the following conditions proposed by Chen and Liu (1990), Habibagahi and Ghahramani (1979) and Scott (1963).

$$\theta_{(1)} = \pi/2 - \varphi, \theta_{(2)} = \pi/2 + \varphi \text{ and } \theta_{(1)} + \theta_{(2)} = \pi \quad (5)$$

Where $\theta_{(1)}$ and $\theta_{(2)}$ are $\angle bjh$ and $\angle bjm$ in Fig. 10 respectively. Accordingly, a theoretical failure mode needs to be corrected based on the test results to satisfy Eq. (5).

First, the potential failure surface of passive zone IV can be considered to be parallel with the theoretical failure surface (β -line_(III)) as it is not affected by the friction characteristics acting on the boundary surface between the soil and the micropile as proposed by Tschebotarioff (1973). Also, the failure surface of zone IV was set as shown in Fig. 10 so that the contained angle $\theta_{(2)}$ in the passive zone satisfies the condition of Eq. (5).

$$v = \xi = \pi/2 - i \quad (6)$$

The test failure surface of the passive zone III was formed wider than the theoretical one. The reason why the failure surface appeared differently was because of the

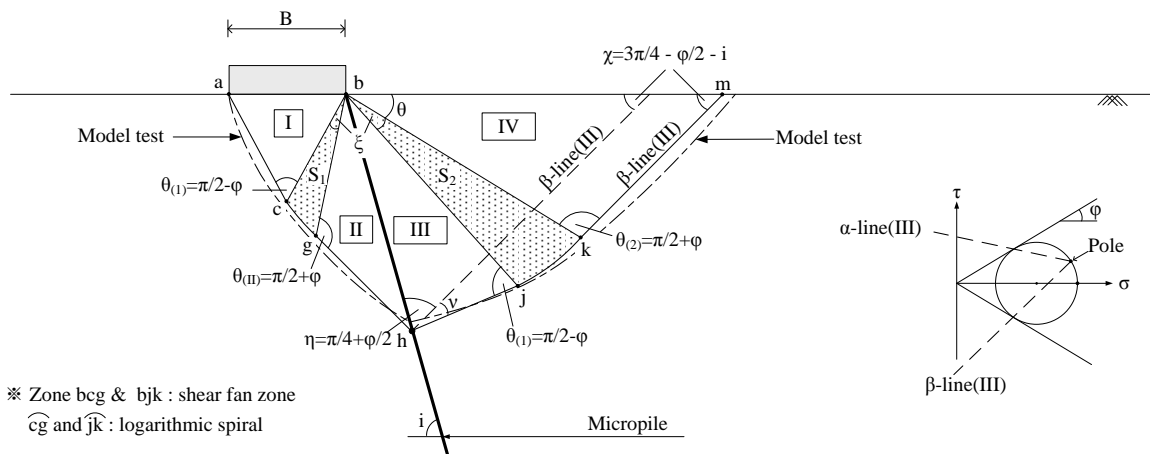


Fig. 10 Analysis of failure surface

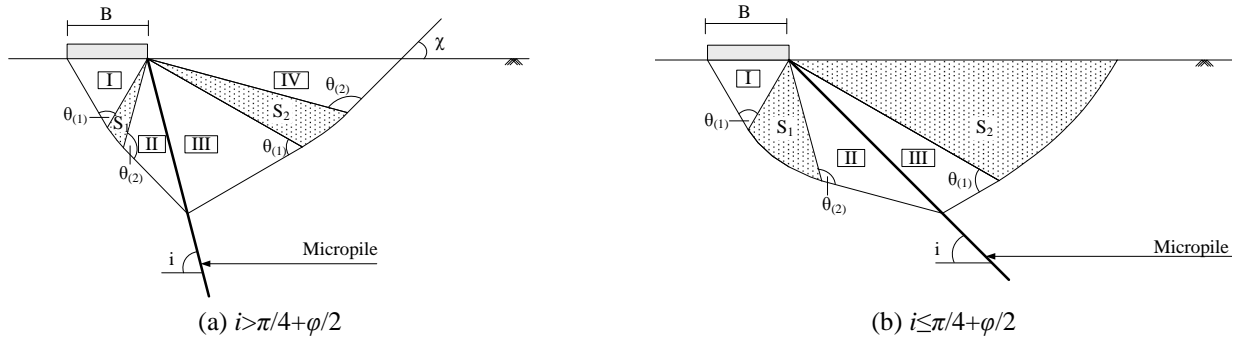


Fig. 11 Failure mechanism of micropiled-raft

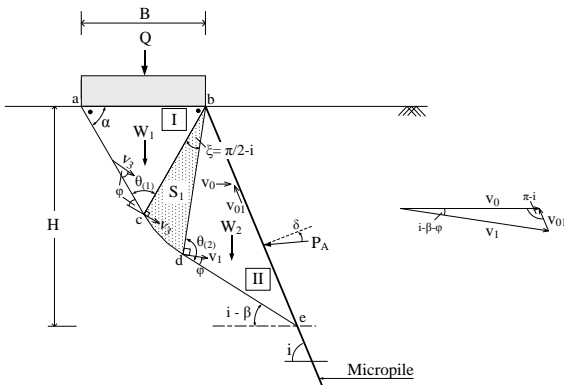


Fig. 12 Failure surface in the active zone

effect of friction acting on the boundary surface between the soil and the micropile. Accordingly, the size of the angle η was obtained considering the geometric characteristics of this zone as shown in Fig. 10. Test results has shown that the angle ν was about $\pi/2-i$, and was equal to the contained angle of the shear fan ($\angle cbg$ in Fig. 10) in an active state. Therefore, the following condition is valid:

The results of the model tests have shown that the actual failure mode varies depending on the installation angle. The shear fan zone increases as the installation angle decreases.

When $2\pi-(\theta_{(2)}-\chi)=0$, zone IV will disappear and only the shear fan zone will exist. In this case, $i=\pi/4+\phi$. Therefore, the cases of the passive zone can be considered in the two categories shown in Fig. 11.

4. Bearing capacity of micropiled-raft

In the upper bound analysis of the limit theorem, the following energy equilibrium equation is valid for the kinematic velocity field during a failure

$$\Delta W_{\text{ext}} = \Delta W_{\text{int}} \quad (7)$$

In order to calculate the bearing capacity, the law of energy conservation can be applied to the failure zone. As the external work carried out by the maximum load, viz. the bearing capacity, is the same as the internal work done in the failure surface, the following equation is valid

$$\Delta W_Q = \sum \Delta W_{(I)} + \sum \Delta W_{(S_1)} + \sum \Delta W_{(II)} + \sum \Delta W_{(III)} + \sum \Delta W_{(S_2)} + \sum \Delta W_{(IV)} \quad (8)$$

The earth pressure relation at the boundary between the micropile and the soil during a failure is as follows

$$P_P \leq P_A \quad (9)$$

P_P and P_A are the passive and active earth pressures at along the micropile respectively. In this case, the vertical load on the foundation Q , which has caused the equilibrium state, represents the bearing capacity.

4.1 Rigid wedge and shear fan

Fig. 12 shows the failure mechanism of the active zone for the failure mode of Fig. 11(a). The weight of the soil in the active state and the work (ΔW_{P_A}) carried out by the active earth pressure can be calculated as follows.

$$\Delta W_{P_A} = \Delta W_{(I)} + \Delta W_{(S_1)} + \Delta W_{(II)} = P_A \cdot v_0 \cdot \sin(i-\delta) \quad (10)$$

$\Delta W_{(I)}$ represents the internal work in zone I, represents the internal work in the shear fan S_1 (logspiral region bcd), $\Delta W_{(II)}$ is the internal work in zone II, v_0 is the translational velocity, and δ is the friction angle between the soil and the micropile. When each term is put in order in Eq. (11), the active earth pressure (P_A) is calculated as follows

$$P_A = \frac{\gamma}{2} \cdot H^2 \cdot \left[\frac{\left\{ \sin^2 \left(\frac{\pi - \phi}{4} \right) \cdot \cos \left(\frac{3\pi - i + \phi}{4} \right) \right\}}{\left\{ \sin(i-\delta) \cdot \sin i \cdot \sin \left(\frac{\pi + \phi}{4} \right) \right\}} \right] + \left[\frac{\cos^2 \left(\frac{\pi + \phi}{4} \right)}{\left\{ \sin i \cdot \cos^2 \phi \cdot \sin \left(\frac{\pi + \phi}{4} \right) \right\}} \right] \times \left[\frac{A_a \cdot \cos \left(\frac{\pi - i + \phi}{4} \right) + B_a \cdot \sin \left(\frac{\pi - i + \phi}{4} \right)}{\sin(i-\delta) \cdot (1 + 9 \cdot \tan^2 \phi)} \right] + \left[\frac{\cos^2 \left(\frac{\pi + \phi}{4} \right) \cdot \sin \left(\frac{\pi - \phi}{4} \right)}{\left\{ \sin(i-\delta) \cdot \sin i \cdot \cos \phi \cdot \sin \left(\frac{\pi + \phi}{4} \right) \right\}} \right]$$

$$\begin{aligned} & \times \exp \left\{ -3 \cdot \left(\frac{\pi}{2} - i \right) \cdot \tan \varphi \right\} \\ & + Q \cdot \frac{\sin i \cdot \sin \left(\frac{\pi}{4} - \frac{\varphi}{2} \right)}{\sin \left(\frac{\pi}{4} + \frac{\varphi}{2} \right)} \cdot \exp \left\{ - \left(\frac{\pi}{2} - i \right) \cdot \tan \varphi \right\} \\ & = \frac{\gamma}{2} \cdot H^2 \cdot K_A + Q \cdot \frac{\sin i \cdot \sin \left(\frac{\pi}{4} - \frac{\varphi}{2} \right)}{\sin \left(\frac{\pi}{4} + \frac{\varphi}{2} \right)} \\ & \times \exp \left\{ - \left(\frac{\pi}{2} - i \right) \cdot \tan \varphi \right\} \end{aligned} \tag{11}$$

Where,

$$\begin{aligned} A_a &= 3 \tan \varphi + \left\{ -3 \tan \varphi \cdot \cos \left(\frac{\pi}{2} - i \right) + \sin \left(\frac{\pi}{2} - i \right) \right\} \\ & \times \exp \left\{ -3 \cdot \left(\frac{\pi}{2} - i \right) \cdot \tan \varphi \right\} \\ B_a &= 1 + \left\{ -3 \tan \varphi \cdot \sin \left(\frac{\pi}{2} - i \right) + \cos \left(\frac{\pi}{2} - i \right) \right\} \\ & \times \exp \left\{ -3 \cdot \left(\frac{\pi}{2} - i \right) \cdot \tan \varphi \right\} \end{aligned}$$

K_A represents the active state earth pressure coefficient, and φ represents the shear resistant angle of soil.

4.2 Rankine passive zone

The failure mode of the passive zone can be considered in two categories as shown in Fig. 11: Case 1 in which $i > \pi/4 + \varphi/2$, Case 2 in which $i \leq \pi/4 + \varphi/2$.

4.1.1 Case 1: $i > \pi/4 + \varphi/2$

Fig. 13 shows the failure mechanism and the displacement velocity field in the failure surface as in Case 1.

The work ($\Delta W_{P(case1)}$) carried out by the passive earth pressure using the failure mode shown in Fig. 13 is as follows

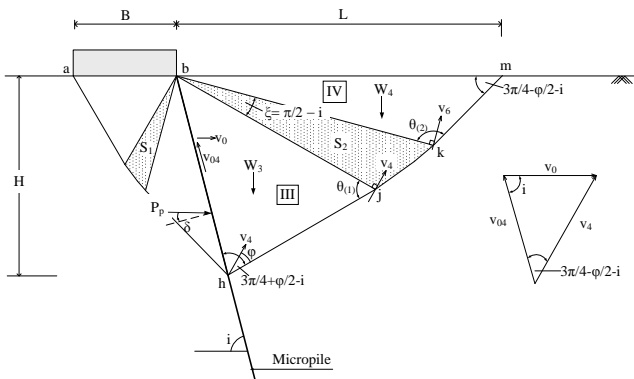


Fig. 13 Failure surface in the passive zone - Case 1 ($i > \pi/4 + \varphi/2$)

$$\Delta W_{P(case1)} = \Delta W_{(III)} + \Delta W_{(S_2)} + \Delta W_{(IV)} = P_P \cdot v_0 \cdot \sin(i + \delta) \tag{12}$$

$\Delta W_{(III)}$ represents the internal work in zone III, $\Delta W_{(S_2)}$ represents the internal work in the shear fan S_2 (logspiral region bjk), and $\Delta W_{(IV)}$ represents the internal work in zone IV. The consequent passive earth pressure ($P_{P(case1)}$) for Case 1 is as follows

$$\begin{aligned} P_{P(case1)} &= \frac{\gamma}{2} \cdot H^2 \cdot \left[\cos \left(\frac{3\pi}{4} - i - \frac{\varphi}{2} \right) \cdot \cos \left(\frac{\pi}{4} - \frac{\varphi}{2} \right) \right. \\ & \times \left. \left\{ \frac{\sin \left(\frac{3\pi}{4} - i + \frac{\varphi}{2} \right)}{\cos \varphi \cdot \sin i \cdot \sin \left(\frac{3\pi}{4} - i - \frac{\varphi}{2} \right)} \right\} \right] \end{aligned} \tag{13}$$

$$\begin{aligned} & + \left\{ \frac{\cos^2 \left(\frac{\pi}{4} + \frac{\varphi}{2} \right)}{\sin i \cdot \cos^2 \varphi \cdot \sin \left(\frac{\pi}{4} + \frac{\varphi}{2} \right)} \right\} \\ & \times \left\{ \frac{A_{P(1)} \cdot \cos \left(\frac{\pi}{4} - \frac{\varphi}{2} \right) + B_{P(1)} \cdot \sin \left(\frac{\pi}{4} - \frac{\varphi}{2} \right)}{1 + 9 \cdot \tan^2 \varphi} \right\} \end{aligned} \tag{13}$$

$$\begin{aligned} & + \left\{ \frac{\sin^3 \left(\frac{3\pi}{4} - i + \frac{\varphi}{2} \right) \cdot \cos \left(\frac{3\pi}{4} - i + \frac{\varphi}{2} \right)}{\sin i \cdot \cos \varphi \cdot \sin \left(\frac{3\pi}{4} - i - \frac{\varphi}{2} \right)} \right\} \end{aligned}$$

$$\times \exp \left\{ 3 \cdot \left(\frac{\pi}{2} - i \right) \cdot \tan \varphi \right\} = \frac{\gamma}{2} \cdot H^2 \cdot K_{P(case1)}$$

$$\begin{aligned} Q_{u(r-case1)} &= \frac{\gamma}{2} \cdot B^2 \cdot (K_{P(case1)} - K_A) \\ & \times \left\{ \frac{\sin^3 \left(\frac{\pi}{4} + \frac{\varphi}{2} \right)}{\sin i \cdot \sin \left(\frac{\pi}{4} - \frac{\varphi}{2} \right) \cdot \cos^2 \left(\frac{\pi}{4} + \frac{\varphi}{2} \right)} \right\} \end{aligned} \tag{16}$$

$$\times \exp \left\{ 3 \cdot \left(\frac{\pi}{2} - i \right) \cdot \tan \varphi \right\} = \frac{\gamma}{2} \cdot B^2 \cdot N_{\gamma(case1)}$$

Where,

$$\begin{aligned} A_{P(1)} &= -3 \tan \varphi + \left\{ 3 \tan \varphi \cdot \cos \left(\frac{\pi}{2} - i \right) + \sin \left(\frac{\pi}{2} - i \right) \right\} \\ & \times \exp \left\{ 3 \cdot \left(\frac{\pi}{2} - i \right) \cdot \tan \varphi \right\} \end{aligned}$$

$$\begin{aligned} B_{P(1)} &= 1 + \left\{ 3 \tan \varphi \cdot \sin \left(\frac{\pi}{2} - i \right) - \cos \left(\frac{\pi}{2} - i \right) \right\} \\ & \times \exp \left\{ 3 \cdot \left(\frac{\pi}{2} - i \right) \cdot \tan \varphi \right\} \end{aligned}$$

$K_{P(case1)}$ is the passive state earth pressure coefficient for Case 1. As $P_A = P_P$ during a failure, the ultimate bearing

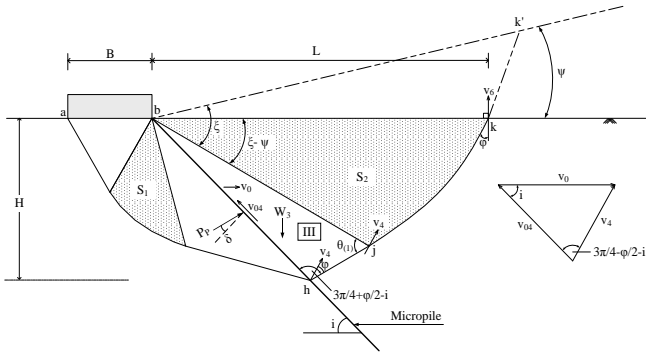


Fig. 14 Failure surface in the passive zone - Case 2 ($i \leq \pi/4 + \varphi/2$)

capacity which is the maximum load is calculated as follows by substituting the relevant parts of Eq. (9) with Eq. (11) and Eq. (13) respectively

$$Q_{u(r-case1)} = \frac{\gamma}{2} \cdot H^2 \cdot (K_{P(case1)} - K_A) \times \left\{ \frac{\sin\left(\frac{\pi}{4} + \frac{\varphi}{2}\right)}{\sin i \cdot \sin\left(\frac{\pi}{4} - \frac{\varphi}{2}\right)} \right\} \exp\left\{\left(\frac{\pi}{2} - i\right) \cdot \tan \varphi\right\} \quad (14)$$

Here, as the width (B) of the raft and the vertical length (H) of the micropile in the soil failure surface are as in Eq. (15) as shown in Fig. 13, the equation can be put in order as follows by substituting the relevant part with Eq. (14).

$$H = B \cdot \sin i \cdot \exp\left\{\left(\frac{\pi}{2} - i\right) \cdot \tan \varphi\right\} \cdot \tan\left(\frac{\pi}{4} + \frac{\varphi}{2}\right) \quad (15)$$

Therefore,

The $N_{\gamma(case1)}$ is the bearing capacity factor of the raft for Case 1.

4.2.2 Case 2. $i \leq \pi/4 + \varphi/2$

Fig. 14 shows the relation between the soil failure mechanism and the displacement field in the failure surface for Case 2.

The passive earth pressure for this case ($P_{P(case2)}$) is put in order as follows by the same way as Case 1

$$\Delta W_{P_{(case2)}} = \Delta W_{(III)} + \Delta W'_{(S_2)} = P_p \cdot v_0 \cdot \sin(i + \delta) \quad (17)$$

$$P_{P(case2)} = \frac{\gamma}{2} \cdot H^2 \cdot \left[\cos\left(\frac{3\pi}{4} - i - \frac{\varphi}{2}\right) \cdot \cos\left(\frac{\pi}{4} - \frac{\varphi}{2}\right) \times \left\{ \frac{\sin\left(\frac{3\pi}{4} - i + \frac{\varphi}{2}\right)}{\cos \varphi \cdot \sin i \cdot \sin\left(\frac{3\pi}{4} - i - \frac{\varphi}{2}\right)} \right\} + \left\{ \frac{\sin i \cdot \sin^2\left(\frac{3\pi}{4} - i + \frac{\varphi}{2}\right)}{\cos^2 \varphi \cdot \sin\left(\frac{3\pi}{4} - i + \frac{\varphi}{2}\right)} \right\} \right]$$

$$\times \left\{ \frac{A_{P(2)}}{1 + 9 \cdot \tan^2 \varphi} \right\} = \frac{\gamma}{2} \cdot H^2 \cdot K_{P(case2)} \quad (18)$$

Where,

$$A_{P(2)} = -3 \tan \varphi + \left\{ 3 \tan \varphi \cdot \cos\left(\frac{\pi}{2} - i - \psi\right) + \sin\left(\frac{\pi}{2} - i - \psi\right) \right\} \times \exp\left\{3 \left(\frac{\pi}{2} - i - \psi\right) \cdot \tan \varphi\right\}$$

$\Delta W_{(S_2)}$ represents the external work in the shear fan S_2 (logspiral region bjk' ; Fig. 14), and $K_{P(case2)}$ represents the passive state earth pressure coefficient for Case 2. Eq. (19) can be put in order as follows by substituting the relevant parts with Eq. (11) and Eq. (18) respectively

$$Q_{(u-case2)} = \frac{\gamma}{2} \cdot H^2 \cdot (K_{P(case2)} - K_A) \times \left\{ \frac{\sin\left(\frac{\pi}{4} + \frac{\varphi}{2}\right)}{\sin i \cdot \sin\left(\frac{\pi}{4} - \frac{\varphi}{2}\right)} \right\} \cdot \exp\left\{\left(\frac{\pi}{2} - i\right) \cdot \tan \varphi\right\} \quad (19)$$

$Q_{u(r-case2)}$ represents the Bearing capacity of the raft in Case 2. On the other hand, Eq. (19) can be put into order as Eq. (20) by substituting the relevant part with Eq. (19).

$$Q_{u(r-case2)} = \frac{\gamma}{2} \cdot B^2 \cdot (K_{P(case2)} - K_A) \times \left\{ \frac{\sin^3\left(\frac{\pi}{4} + \frac{\varphi}{2}\right)}{\sin i \cdot \sin\left(\frac{\pi}{4} - \frac{\varphi}{2}\right) \cdot \cos^2\left(\frac{\pi}{4} + \frac{\varphi}{2}\right)} \right\} \times \exp\left\{3 \left(\frac{\pi}{2} - i\right) \cdot \tan \varphi\right\} = \frac{\gamma}{2} \cdot B^2 \cdot N_{\gamma(case2)} \quad (20)$$

$N_{\gamma(r-case2)}$ represents the bearing capacity factor of the raft in Case 2.

5. Validation and discussion

5.1 Validation of bearing capacity equations

In order to verify the proposed bearing capacity formula, a series of separate model tests were conducted. Fig. 15 shows the load displacement relation of the model test. Though, the bigger the installation angle is, the more the early stage bearing capacity is taken by the micropile. As the soil deformation progresses, the soil confining effect is reflected and the bearing capacity contributed by the raft has increased.

In Fig. 16(a), the bearing capacity calculated using the bearing capacity formula of Eq. (16) and Eq. (20) are presented in this paper and compared with the test results. The effect of the installation angle of the micropiled-raft

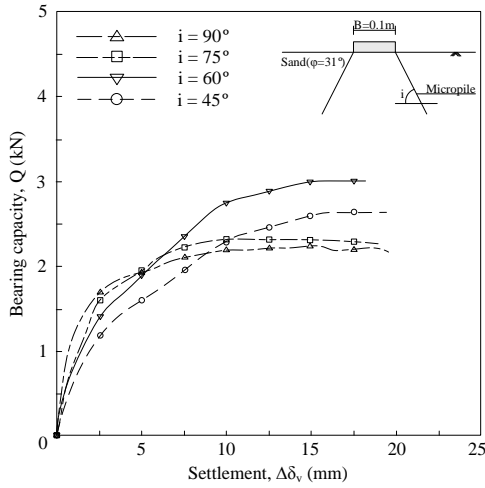
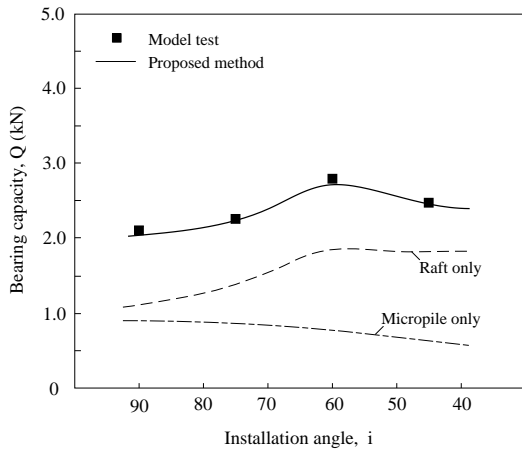
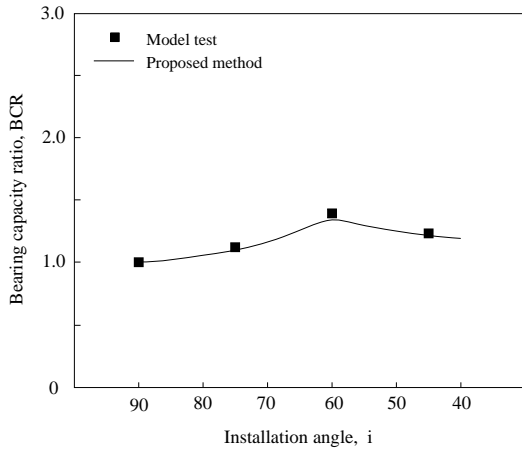


Fig. 15 Load-displacement relationship of model test



(a) Bearing capacity of micropiled-raft



(b) Bearing capacity ratio (BCR)

Fig. 16 Comparison of bearing capacity

system is also investigated. To describe the interaction between the micropile and soil effectively, the concept of bearing capacity ratio (BCR) is introduced as follows

$$\text{Bearing capacity ratio(BCR)} = \frac{Q_{u(\text{mp}; i < 90^\circ)}}{Q_{u(\text{mp}; i = 90^\circ)}} \quad (21)$$

This parameter enables the effect of the installation

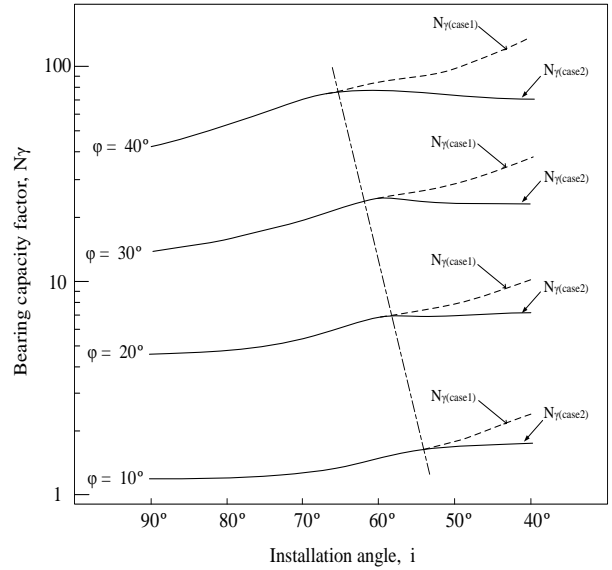


Fig. 17 Design chart for N_γ

angle of the micropile to be easily identified. As shown in Fig. 16(b), the bearing capacity has increased as the installation angle increased at the beginning, and then decreased when the installation angle exceeded 60°. The bearing capacity when the micropile angle was 60° showed an increase of about 20% in comparison to that when the piles were vertically installed. This means that the soil confining effect of the micropile is at maximum when the installation angle is about 60°.

5.2 Design chart and discussions

As the bearing capacity formulas in Eqs. (16) and (20) are complicated, it seems to be cumbersome to calculate the bearing capacity using the formula at all times. It would be useful to provide a chart for a bearing capacity coefficient for actual application to design. In Fig. 17, the coefficient of the bearing capacity formula proposed is expressed in terms of installation angle and angle of shear resistance.

The above design chart is aimed at application to strip footing. However, additional verification would be required through a field loading test. It would be desirable to apply the above equations to the preliminary design. The total bearing capacity of the micropiled-raft system can be obtained by combining the bearing capacity of micropiles using Eq. (1) of which the first term is in the right hand side, with that of the micropiled-raft using the design chart shown in Fig. 17.

6. Conclusions

This study has presented the bearing capacity of the micropiled-raft system. In order to identify the bearing capacity mechanism of the micropiled-raft system, a numerical simulation was conducted. The results of the numerical analyses showed that the bearing capacity of the micropiled-raft system can be seen as the sum of the contribution of the micropile as a slender pile to the bearing

capacity, and the bearing capacity of the raft on which the soil reinforcement effect is reflected.

The load resistance mechanism of the micropiled-raft system has also been identified using both the numerical method and physical model tests. It is revealed that the micropile reaches the yield state first and, while it maintains a certain bearing capacity, as a slender pile beneath the raft. The confining effect of the micropile contributes to increase in the bearing capacity of soils.

A bearing capacity equation based on the upper bound analysis of the limit theorem was proposed. For the bearing capacity of the micropiled-raft system, the pile installation angle was shown to be a crucial factor, and an installation angle of about 60° was shown to be mechanically most advantageous. The proposed bearing capacity formula was verified through separate model tests, and showed to be well agreeable to the test results. For convenience of application, the bearing capacity coefficients were presented using a design chart in terms of installation angle and angle of shear resistance of soils. The proposed bearing capacity formula will be useful for the preliminary design of the micropiled-raft system. However, as the proposed bearing capacity equation is basically based on the model tests, it would be desirable to use the equation just on a preliminary study of the project, and further study including field measurements would be required for the practical design application.

Acknowledgments

The preparation of this paper was supported by the National Research Foundation of Korea under Research Project 2015R1A2A1A05001627. The authors greatly appreciate the supports provided.

References

- Alnuaim, A.M., El Nagger, H. and El Naggar, M.L. (2015), "Performance of micropiled raft in sand subjected to vertical concentrated load: centrifuge modeling", *Can. Geotech. J.*, **52**(1), 33-45.
- Chen, W.F. (1975), *Limit Analysis and Soil Plasticity: Developments in Geotechnical Engineering 7*, Elsevier, New York, USA.
- Chen, W.F. and Liu, X.L. (1990), *Limit Analysis in Soil Mechanics*, ELSEVIER, Amsterdam, Netherlands.
- Chen, Y.H., Chen, L., Xu, K., Liu, L. and Ng, C. (2013), "Study on critical buckling load calculation method of piles considering passive and active earth pressure", *Struct. Eng. Mech.*, **48**(3), 367-382.
- Colmenares, J.E., Kang, S.R., Shin, Y.J. and Shin, J.H. (2014), "Ultimate bearing capacity of conical shell foundations", *Struct. Eng. Mech.*, **52**(3), 507-523.
- Das, B.M. (2011), *Principles of Foundation Engineering*, CENGAGE Learning, USA.
- FHWA (2005), *Micropile Design and Construction*, United States Department of Transportation, No. FHWA NHI-05-039, December, USA, 3-11-3-22.
- Francis, J. (1964), "Analysis of pile group with flexible resistance", *J. Soil Mech. Found.*, ASCE, **90**(3), 3887-3891.
- Habbibagahi, K. and Ghaharmani, A. (1979), "Zero extension theory of earth pressure", *J. Geotech. Geoenviron. Eng.*, ASCE, **105**(7), 881-896.
- Han, J. and Ye, S.L. (2006), "A field study on the behavior of a foundation underpinned by micropiles", *Can. Geotech. J.*, **43**(1), 30-42.
- Harr, M.E. (1966), *Foundations of Theoretical Soil Mechanics*, McGRAW-Hill, New-York, USA.
- Hoalley, P.J., Francis, A.J. and Stevens, L.K. (1969), "Load testing of slender steel pile in soft clay", *Proceeding of 7th International Conference Soil Mechanics and Foundation Engineering*, Mexico city, Mexico, August.
- Holman, T.P. (2009), "Behavior and mechanics of micropiles in rock", *Proceeding of the 17th International Conference on Soil Mechanics and Geotechnical Engineering*, Alexandria, Egypt, October.
- Hwang, T.H., Kim, K.H. and Shin, J.H. (2017), "Effective installation of micropiles to enhance bearing capacity of micropiled raft", *J. Soil. Found.*, **57**, 36-49.
- Iai, S. (1989), "Similitude for shaking table tests on soil-structure-fluid model in 1g gravitational field", *J. Soil. Found.*, **29**(1), 105-111.
- Iai, S., Tobita, T. and Nakahara, T. (2005), "Generalised scaling relations for dynamic centrifuge tests", *Geotechniq.*, **55**(5), 355-362.
- Kyung, D. and Lee, J. (2017), "Uplift load-carrying capacity of single and group micropiles installed with inclined conditions", *J. Geotech. Geoenviron. Eng.*, ASCE, **143**(8), 04017031.
- Lamb, T.W. and Whitman, R.V. (1979), *Soil. Mechanics: SI Version*, JOHN WILEY & SONS, New York, USA.
- Meyerhof, G.G. (1995), "Behavior of pile foundations under special loading conditions", *Can. Geotech. J.*, **32**(2), 204-222.
- Meyerhof, G.G. and Yalcin, A.S. (1993), "Behavior of flexible battered piles under inclined load in layered soil", *Can. Geotech. J.*, **30**(2), 247-256.
- Pinyol, N.M. and Alonso, E.E. (2012), "Design of micropile for tunnel face reinforcement: undrained upper bound solution", *J. Geotech. Geoenviron. Eng.*, ASCE, **138**(1), 89-98.
- Polous, H.G. (2001), "Piled raft foundation: design and application", *Geotechnique*, **51**(2), 95-113.
- Poulos, H.G. and Davis, E.H. (1980), *Pile Foundation Analysis and Design*, John Wiley & Sons, INC., New York.
- Randolph, M.F. (1994), "Design method for pile groups and piled raft", *Proceeding of the 13th International Conference Soil Mechanics and Foundation Engineering*, New Delhi, India, January.
- Reul, O. and Randolph, M.F. (2003), "Piled raft in overconsolidated clay: comparison of in situ measurements and numerical analyses", *Geotechniq.*, **53**(3), 301-315.
- Saha, R., Dutta, S. and Haldar, S. (2015), "Effect of raft and pile stiffness on seismic response of soil-piled raft-structure system", *Struct. Eng. Mech.*, **55**(1), 161-189.
- Salisbury, N.G. and Davidow, S.A. (2014), "Current design and construction practices for micropile supported foundations of electrical transmission structures in North America", *12th Int. Workshop on Micropiles*, International Society for Micropile, Eighty Four, PA.
- Sanctis, L.D. and Mandolini, A. (2006), "Bearing capacity of piled rafts on soft clay soils", *J. Geotech. Geoenviron. Eng.*, ASCE, **132**(12), 1600-1610.
- Scott, R.F. (1963), *Principal of Soil Mechanics*, Addison-Wesley Publishing Co., INC., Massachusetts, USA.
- Shu, S. and Muhunthan, B. (2010), "Influence of sand state on network effect of micropile", *Proceedings of the 10th International Society for Micropiles Workshop*, Washington, USA, September.
- Sun, S.W., Zhu, B.Z. and Wang, J.C. (2013), "Design method for stabilization of earth slope with micropile", *J. Soil. Found.*,

53(4), 487-497.

Tschebotarioff, G.P. (1973), *Foundation, Retaining and Earth Structures: The Art of Design and Construction and Its Scientific Basis in Soil Mechanics-Second Edition*, McGRAW-Hill KOGAKUSHA LTD., Tokyo, Japan.

Tsukada, Y., Miura, K., Tsubokawa, Y., Otani, Y. and You, G. (2006), "Mechanism of bearing capacity of spread reinforcing with micropile", *J. Soil. Found.*, **46**(3), 367-376.

You, G.L., Miura, K. and Ishito, M. (2003), "Behavior of micropile foundation under inclined loads in laboratory tests", *Lowland Tech. Int.*, **5**(2), 16-26.

CC